

Full Length Article

Analyzing thermal maturity effect on shale organic matter via PeakForce quantitative nanomechanical mapping



Chioma Onwumelu^{a,*}, Oladoyin Kolawole^b, Stephan Nordeng^a, Olufemi Olorode^c

^a Harold Hamm School of Geology and Geological Engineering, University of North Dakota, Grand Forks, ND, 58202, USA

^b John A. Reif, Jr. Department of Civil and Environmental Engineering, New Jersey Institute of Technology, Newark, NJ, 07102, USA

^c Craft and Hawkins Department of Petroleum Engineering, Louisiana State University, Baton Rouge, LA, 70803, USA

ARTICLE INFO

Keywords:

Rock mechanics
Nanomechanics
Shale
Organic matter
Atomic force microscopy
Nanomechanical mapping

ABSTRACT

Organic-rich shales have gained significant attention in recent years due to their pivotal role in unconventional hydrocarbon production. These shale rocks undergo thermal maturation processes that alter their mechanical properties, making their study essential for subsurface operations. However, characterizing the mechanical properties of organic-rich shale is often challenging due to its multiscale nature and complex composition. This work aims to bridge that knowledge gap to fully understand the nanomechanical properties of Shale organic matter at various thermal maturation stages. This study employs PeakForce Quantitative Nanomechanical Mapping (PF-QNM) using Atomic Force Microscopy (AFM) to investigate how changes at the immature, early mature, and peak mature stages impact the mechanical properties of the Bakken Shale organic matter. PF-QNM provides reliable mechanical measurements, allowing for the quantification and qualification of shale constituents' elastic modulus (E). We also accounted for the effect of probe type and further analyzed the impact of probe wear on the nanomechanical properties of shale organic matter. In immature shale, the average elastic modulus of organic matter is approximately 6 GPa, whereas in early mature and peak mature shale, it decreases to 5.5 GPa and 3.8 GPa, respectively. Results reveal a mechanical degradation with increasing thermal maturation, as evidenced by a reduction in Young's modulus (E). Specifically, the immature shale exhibits an 8% reduction in E , while the early mature and peak mature shales experience more substantial reductions of 31% and 37%, respectively. This phenomenon could be attributed to the surface probing of low-modulus materials like bitumen generated during heating. The findings underscore the potential of AFM PF-QNM for assessing the nanomechanical characteristics of complex and heterogeneous rocks like shales. However, it also highlights the need for standardized measurement practices, considering the diverse components in these rocks and their different elastic moduli.

1. Introduction

Organic-rich shales were poorly studied a few decades ago, mainly due to low economic importance and complex geophysical responses observed in the subsurface. However, this has changed over the last two decades because of the realization that organic-rich shales are essential elements in producing unconventional plays. More research efforts have focused on understanding the multi-scale mechanical properties and behavior of rocks, especially low-permeable rocks (Olorode et al., 2020; Kolawole and Oppong, 2023; Ngoma and Kolawole, 2024). Organic matter undergoes thermal maturation, which involves chemical and physical processes that change the physical properties of the whole rock (Onwumelu et al., 2021, 2023). Several geological factors can shape and

influence rock formation over millions of years. Furthermore, human intervention via extensive and continuous production alters rock properties, giving rise to more complex and coupled physical processes in the rock. Maximizing hydrocarbon production is a continuous quest as the production in many wells tends to decline over time. Thus, there is a constant need to analyze subsurface rocks across scales, ranging from nanoscale measurements to field and basin scales. One benefit of nanoscale measurements of organic-rich shale rock properties is the ability to obtain experimental measurements on rock samples small enough to avoid potentially breaking these fissile rocks, which are known to break easily at the centimeter scale.

Ulm and Abousleiman (2006) are among the foremost proponents of nanoscale measurements in shales. Their study illustrated that the

* Corresponding author.

E-mail address: chioma.onwumelu@und.edu (C. Onwumelu).

<https://doi.org/10.1016/j.rockmb.2024.100128>

Received 3 March 2024; Received in revised form 15 April 2024; Accepted 2 May 2024

2773-2304/© 2024 Chinese Society for Rock Mechanics & Engineering. Publishing services by Elsevier B.V. on behalf of KeAi Co. Ltd. This is an open access article under the CC BY-NC-ND license (<http://creativecommons.org/licenses/by-nc-nd/4.0/>).

nanogranular packing density of the rock governs the mechanical properties. Additionally, statistical analysis of nanoindentation tests allows the determination of the mechanical microstructure, which is useful in upscaling the micromechanical modeling to a macroscale understanding of rock behavior (Bobko and Ulm, 2008). However, there is usually a need to couple the experiment with scanning electron microscope (SEM) imaging and energy dispersive X-ray spectroscopy (EDS) to observe which rock components are targeted during testing. Mechanical and petrophysical rock properties are essential for subsurface operations and exploitation, but the mechanical properties of organic-rich shales are challenging to characterize due to some critical factors. Fender et al. (2020) reported that organic-rich shales present two significant challenges. These include the often-overlooked multiscale nature of shale and the need to understand the factors or parameters that control the mechanical properties of shale. Bobko & Ulm (2008) detailed the role of nanoscale and microscale properties in controlling mechanical behavior and shale anisotropy. Additionally, pore size distribution and fracture networks contribute to the mechanical properties of shale at the micro- and nanoscale. Shale grain size is variable and may include grains as small as 1 nm or as large as 100 μm .

Nanoindentation and Atomic Force Microscopy (AFM) capture the mechanical properties of every mineral present in the rock at very small length scales and can be used to characterize their microstructure. Nanoindentation measurements on organic-rich shales provide a good approximation of the bulk elastic properties of shale when using high-load measurements.

There are only a few published data available on the elastic properties of kerogen. Studies such as Zargari et al. (2016) show that kerogen properties change with thermal maturation. In Bakken Shales, for example, it has been observed that immature shales typically have a high Young's modulus (stiffness), and the Young's modulus reduces as the shales become more thermally mature. Minerals have also been observed to affect the mechanical properties of shales. Shales with high carbonate and quartz content tend to have high values of Young's modulus. Minerals in sedimentary rocks undergo diagenetic processes and chemical reactions that change their mechanical properties compared to the mechanical properties of minerals in igneous rocks or ideal crystals (Graham et al., 2021). However, thermal maturation remains a significant factor in the diagenesis and catagenesis of organic-rich shales because it alters their overall rock microstructure and strength.

Few studies have related the mechanical properties of organic matter with maturation. The elastic properties and spatial distribution of organic matter are pivotal in unconventional shales due to their significance in shaping the rock's overall mechanical characteristics. This holds immense importance in multiple aspects, such as processing seismic data to derive elastic modulus and simulating fracture propagation, highlighting the critical role of organic matter in these processes (Avseth et al., 2010; Dahi-Taleghani and Olson, 2011; Gale et al., 2014). There is growing interest in understanding the mechanical properties of individual components in shales (including the organic matter and inorganic minerals) at the microscale and nanoscale because shales typically vary in the relative amounts of these different components (Alstadt et al., 2016; Khatibi et al., 2018; Li et al., 2018; Liu et al., 2018; Mavko et al., 2020). Khatibi et al. (2018) used Raman spectroscopy to relate the kerogen molecular structure change with maturation. Raman spectroscopy involves using a laser beam to excite the molecules and atoms on the sample surface and measuring the wavelength response related to the chemical composition and structure. In their study, they proposed a correlation to indirectly obtain Young's modulus from the band separation of the Raman spectroscopy method and vitrinite reflectance R0%. The study suggests that Young's modulus increases as R0% increases. Another theoretical modeling study (Kong et al., 2018) showed the opposite results to that of Khatibi et al. (2018), by demonstrating that the kerogen mechanical properties decrease with maturity. Therefore, further investigations are necessary to better understand the change in the mechanical properties of organic matter with thermal maturation.

AFM is an effective method for identifying the mechanical characteristics of materials at the nanoscale. It yields a high-resolution quantitative mechanical map when the AFM PeakForce Quantitative Nanomechanical Mapping (PF-QNM) mode is used. The modulus of a material is calculated from the force-displacement curve. Precisely, the deflection of the AFM cantilever is measured after a constant peak force is applied to a very fine tip, typically with a radius smaller than 100 nm (Sedin and Rowlen, 2001). The subsequent phase estimates the Derjaguin-Muller-Toporov (DMT) modulus by deriving the force-displacement curve for every nanometer-scale pixel throughout the scanning process. (Derjaguin et al., 1975). The force-displacement curve can also yield parameters, such as topography, deformation, adhesion, and dissipation. This method has been widely used to mechanically characterize biological materials, cement, and polymers (Asgari et al., 2018; Niu et al., 2016; Wang et al., 2014).

Kong et al. (2021) used AFM and nanoindentation methods to study the nanomechanical properties of four Bakken shale (in the pre-oil window) samples. Similarly, Graham et al. (2021) used AFM and nanoindentation methods to study the nanoscale mechanical properties of two organic-rich calcareous shales (dry gas window). The focus of the study was on the siliciclastic end-member minerals, so they did not account for the maturity of the organic-rich shale samples. Li et al. (2018) used AFM PF-QNM to characterize the nanomechanical properties of the organic matter of the Bakken Shale but did not consider its thermal maturity. They suggested that the heterogeneity in the elastic properties of organic matter might be due to thermal maturity, which was not incorporated in the study. Abedi et al. (2016a, 2016b) studied the role of thermal maturity and organic matter content on shale microtextural evolution, using grid nanoindentation and energy-dispersive X-ray spectroscopy (EDX). The results suggest that shales with organic matter and clay particles may show consistent mechanical responses that are unrelated to their maturity and total organic content (TOC). Also, in the study, the elasticity values for illite correlate well with the results obtained from molecular simulations.

The use of AFM PF-QNM in this study will enable us to examine the spatial variations in mechanical properties at the nanometer scale across a surface without the influence of the underlying phase (Pittenger et al., 2010). Few studies have used this technique to evaluate the mechanical properties of shale components for either the organic or inorganic phase. The first use of this approach on shale samples was documented by Eliyahu et al. (2015). Emmanuel et al. (2016) also investigated the effects of thermal maturity on the elastic properties of the organic matter using the AFM PF-QNM on Cretaceous shales. The study showed that the elastic modulus tends to increase as thermal maturity increases and that organic matter softens at high values of reservoir temperature. Using the same methodology, Li et al. (2018) investigated how thermal maturity affected the mechanical characteristics of solid bitumen. Hence, it is valuable to investigate the influence of thermal maturity on the mechanical characteristics of organic matter within shale at the sub-core scale.

In this study, the fine-scale (nanoscale) mechanical properties of Bakken Shale organic matter will be investigated using the PeakForce Quantitative Nanomechanical Mapping (PF-QNM) technique in atomic force microscopy (AFM). The goal of this study is to: (i) understand how changes at the immature, early mature, and peak mature stages impact the mechanical properties of the Shale rocks (specifically Bakken shale); (ii) investigate the effect of probe type on the nanomechanical characterization and the results of AFM in organic-rich shale.

2. Experimental methods

2.1. Sample preparation (thermal maturation experiment)

A 1 kg shale rock core was taken from a well (as indicated on the map of North Dakota, USA), shown in Fig. 1. The core was taken at the depth of the Bakken Formation and used for all the experiments. Each experiment involved placing 2.5 g of the sample in a 6-inch stainless steel,

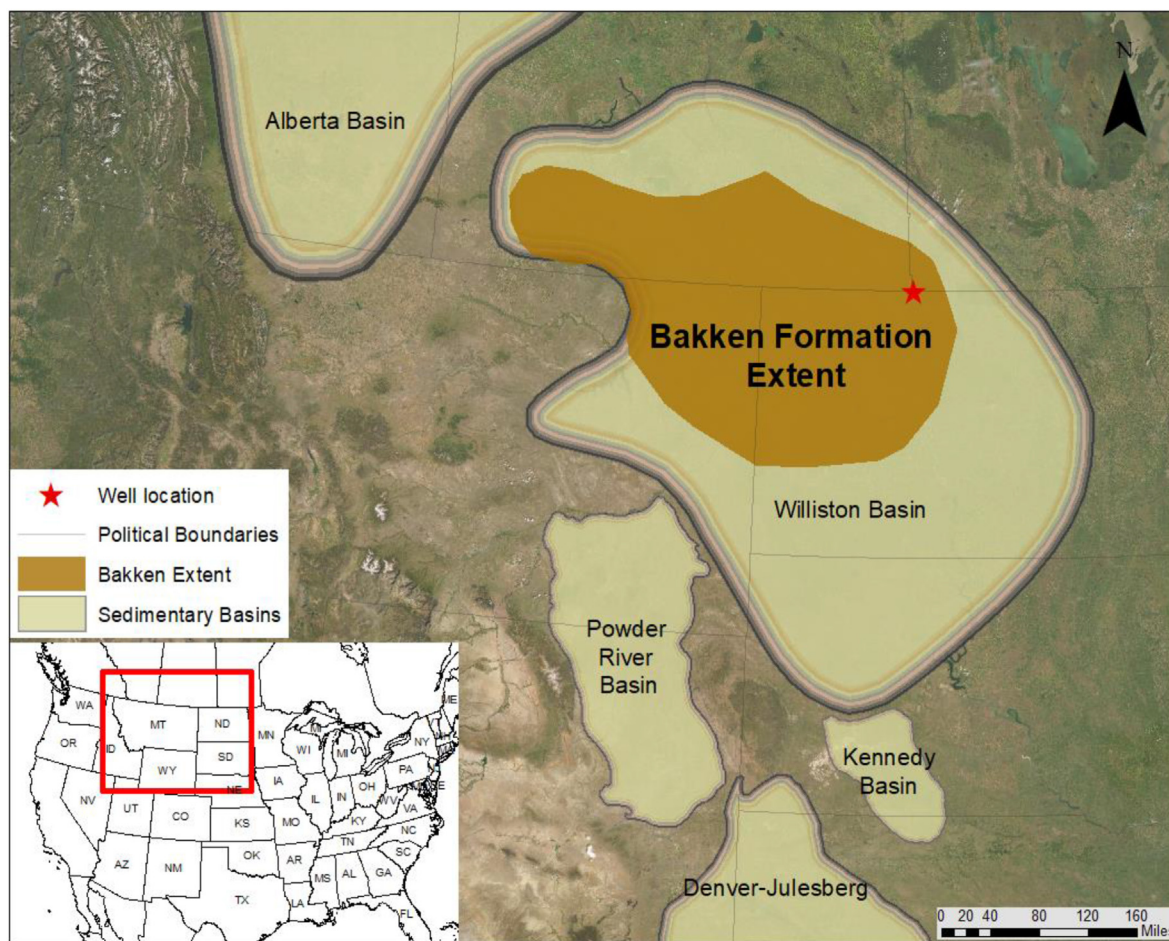


Fig. 1. The extent of the Williston Basin and the extent of the Bakken Formation. The red star is the location of the sampled well (2-BRENDE 9-33 1-M, NDIC # 24,883). Modified from (Gerhard et al., 1982). (For interpretation of the references to colour in this figure legend, the reader is referred to the Web version of this article.)

hydrothermal reaction vessel with 10 mL distilled water and a headspace filled with Helium. The vessels were heated in a muffle furnace oven at 340 °C for 12 h and 48 h to simulate the thermal breakdown of the source rock kerogen. The T_{max} of 444 °C was achieved at 48 h, close to the maximum recorded T_{max} of 445 °C in the Williston Basin. The resulting solid reaction products were obtained by filtering and washing with distilled water.

2.2. Source rock analysis (Rock-Eval equivalent)

The experimental samples were crushed and analyzed with a source-rock analyzer (SRA). The process involved placing the crushed samples in a crucible, which was then transferred to the SRA pedestal and raised to a temperature of 300 °C oven. The sample was maintained at this temperature for 3 min, during which free hydrocarbons were volatilized. These volatilized hydrocarbons are detected by the flame ionization detector (FID) detector and measured in milligrams (mg/HC) of free hydrocarbon (S_1) per gram of rock. Free CO_2 was also released (referred to as S_3), measured simultaneously using an IR cell, and reported in milligrams (mg/ CO_2) per gram of rock up to a temperature of 400 °C.

The temperature was ramped to 650 °C at a rate of 25 °C per minute. At this point, hydrocarbons were generated from the pyrolytic degradation of the kerogen, detected by the FID detector, and reported in milligrams (mg/HC) of crackable hydrocarbon (S_2) per gram of rock (Fig. 2). After the pyrolysis, the oven was cooled below 650 °C to prevent any pyrolysis components from being released because of oxidation. The oven was then maintained at isothermal conditions of 580 °C while the

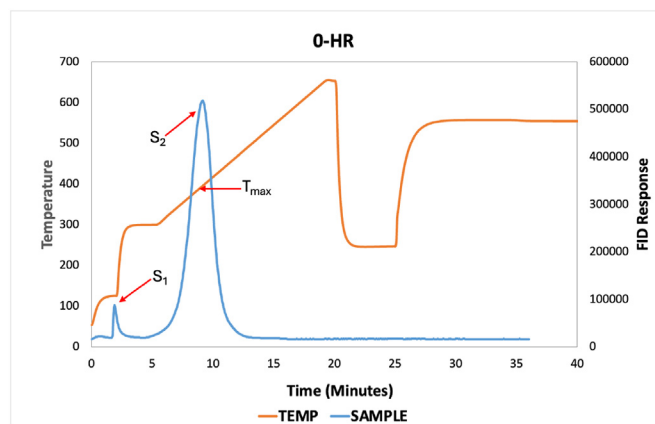


Fig. 2. Illustration of Source-rock analysis from 0-hr sample. T_{max} is the temperature at maximum hydrocarbon generation.

sample was purged with air to oxidize the remaining residual organic carbon. During this time, carbon monoxide (CO) and CO_2 were measured with the IR cells to determine the residual carbon content (S_4).

This pyrolysis process provided valuable geochemical properties such as the total organic carbon (TOC), thermal maturity (T_{max}), free hydrocarbon (S_1), crackable hydrocarbon (S_2), hydrogen index (HI), and oxygen index (OI).

2.3. X-ray diffraction

The reaction products from the 0, 12 h, and 48 h samples were ground to a size of less than 1 mm. Approximately 4 g of the samples were also crushed and powdered to less than 2 μm using a McCrone micronizing mill. Care was taken to clean the equipment between samples to avoid cross-contamination. The sample powder was lightly loaded into a frontload holder and subjected to scanning using a Bruker D2 PHASER XRD analyzer. The scans utilized Cu K α radiation and a LYNXEYE XE-T detector, covering a range from 4° to 80° 2 θ with a step size of 0.01°. A software (DIFFRAC.EVA from Bruker) was used to identify the mineral phases in each sample, using the open crystallographic database (COD). To minimize potential errors stemming from sample preparation methods, the analyses were conducted three times.

2.4. Atomic force microscopy (AFM)

2.4.1. Sample preparation

Roughly 1 × 2 × 0.5 cm of each sample was placed in a 2.5 cm diameter mold and then embedded in a combination of Epo-Thin® epoxy and hardener before curing for 24 h. Grinding and polishing wheels (LaboPol-5, Struers) were used to prepare the embedded samples for subsequent characterization. An 800-grit silicon carbide paper was used to create a flat bottom and carefully expose the shale. The surface of the shale was flattened with 1200-grit silicon carbide paper. Finally, a polishing pad with progressively finer solutions was used to complete the surface preparation down to a final 0.5 μm colloidal silica solution. After each grinding/polishing step, each sample was lightly rinsed and air-dried to remove any residual abrasives. To identify the same regions of interest across characterization methods, we selected optically identifiable origins, and recorded stage movements with sub-micrometer precision.

It is essential to have a very smooth sample for quantitative nanoscale mechanical property analysis. Unfortunately, the Bakken shale has a soft matrix with more complex mineral grains embedded in it. This results in differential polishing, grain plucking, and smearing of the softer matrix material, making its mechanical sample preparation difficult. By using an incremental process, we minimized the adverse effects associated with mechanical polishing. The AFM characterization was performed at the Micron School of Materials Science and Engineering, Boise State University, using PF-QNM mode on a Dimension Icon AFM platform (Bruker).

Three regions of interest (ROI) were selected to better represent the organic matter (concentration of dark areas) in the samples. Selecting multiple ROI across each sample allows for a more comprehensive understanding of the spatial variations in mechanical properties, particularly concerning organic-rich regions. Table 1 presents the samples used and their conditions.

2.4.2. Characterization using PF-QNM

For the PF-QNM technique to provide quantitative results, three primary instrument parameters must be calibrated: the cantilever spring constant, deflection sensitivity, and tip radius. The probe's cantilever

Table 1
Sample condition.

Sample	Condition	Additional Information
0-hr	Immature stage; No heating	All tests were conducted on three different regions of interest (ROI) for each sample = ROI 1, ROI 2, and ROI 3
12-hr	Early mature stage; Heated for 12 h	
48-hr	Peak-mature stage; Heated for 48 h	

spring constant (k) is worth considering because it can limit the effective range of moduli the probe can reliably measure. To calibrate the cantilever spring constant, laser doppler vibrometry is used at the factory to provide accurate values that are unique to each probe. The deflection sensitivity (DS) relates the signal output from the photosensitive diode to the displacement of the cantilever and is measured in nm/V. By using a very stiff material (such as sapphire), we ensured that any measured deformation was the direct result of the cantilever displacement, leading to accurately calibrated values. Finally, the tip radius was used to calculate the contact area, stress, and elastic modulus. To ensure that the diamond tip does not wear or become damaged, a Titanium roughness standard is used to create a 3D model of the tip. The Titanium standard has extremely sharp needle-like features perpendicular to the surface, which are smaller than the probe tip radius. This size difference allows the features to image the tip instead of the tip imaging the surface. Using an implementation of the blind tip reconstruction method in appropriate software algorithms, the tip radius can then be extracted from the resulting topography images.

The probe's cantilever spring constant is a material property that does not change significantly throughout its lifetime. Thus, the factory-calibrated values are typically used for any quantitative analysis. However, the deflection sensitivity is system-dependent and must be measured for each experiment. The tip radius can also change over time, so it is checked before each experiment.

Due to the stiffness of the shale matrix and expected mineral inclusions, Bruker PDNISP probes were chosen to image the samples. Although the diamond tip of the PDNISP probes could reduce lateral resolution because of their low aspect ratio, it offers unmatched durability, which is necessary when taking multiple images across samples. Prior to experimental measurements of the elastic moduli, a PF-QNM image was taken on a highly ordered pyrolytic graphite (HOPG) standard (Bruker, HOPG-12 M). HOPG has a nominal elastic modulus of 18 GPa and was used to select an appropriate probe tip radius during post-processing. After all the appropriate parameters were calibrated, each sample was loaded onto the AFM stage and brought directly beneath the mounted probe tip. Using the AFM's integrated optical microscope, a distinct feature was chosen to be the origin from which stage movement could be measured. This facilitated colocalization with SEM. Three regions of interest were identified (on each sample) and imaged using similar PF-QNM parameters. During the imaging, each tip-sample interaction was measured and saved as a force-displacement curve. This enabled post-processing using AtomicJ (Hermanowicz et al., 2014), an open-source software.

The small size of the mineral inclusions and the broad range of the expected moduli make PF-QNM capable of probing the mechanical properties of shale. In PF-QNM, an AFM probe oscillates well below its resonant frequency while scanning the sample's surface. For each tip-sample interaction, a force-displacement curve is generated. The difference between the user-defined peak force setpoint and the measured peak force is used as a feedback signal to maintain tracking. In real-time, the force-displacement data are fitted using the Derjaguin-Muller-Toporov (DMT) contact mechanics model (Derjaguin et al., 1975) to calculate the reduced elastic modulus, E^* . In addition, parameters such as the height of the sensor, deformation, and dissipation can also be derived from the entire force-displacement curve, as shown in Fig. 3.

The reduced modulus (E^*) can be calculated from the following equation (Derjaguin et al., 1975):

$$F = \frac{4}{3}E^* \sqrt{R\delta^3} + F_{adh} \quad (1)$$

where F is the applied force, E^* is reduced modulus (DMT modulus), R is the radius of the probe tip, δ is the indentation depth, and F_{adh} is the adhesion force. The Young's modulus of the sample can be calculated as

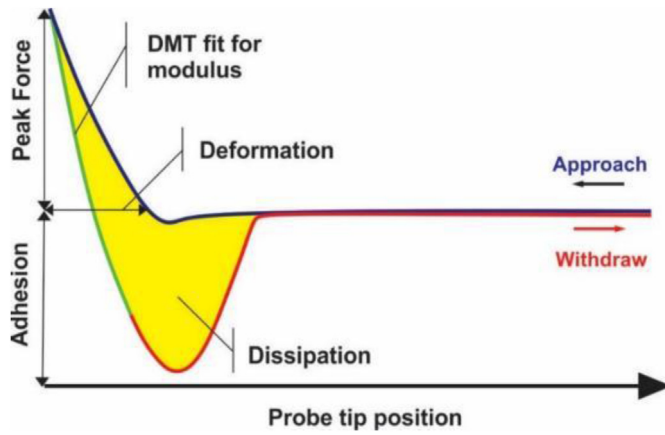


Fig. 3. Schematic diagram of an entire force-distance curve. Modified from (Hua, 2014).

follows:

$$E^* = \frac{1}{\frac{1 - \nu_s^2}{E_s} + \frac{1 - \nu_{tip}^2}{E_{tip}}} \quad (2)$$

where ν_s is Poisson's ratio of the sample, E_s is Young's modulus of the sample, ν_{tip} is Poisson's ratio of the probe, and E_{tip} is Young's modulus of the probe. The Poisson's ratio and Young's modulus of the probe can be obtained from the manual (Hua, 2014).

2.4.3. Data analysis

Each AFM image consists of 512×512 pixels, yielding 262,144 force-displacement curves per image. A software, AtomicJ (Hermanowicz et al., 2014), was used to batch analyze all the force-displacement curves because the large data size makes it impractical to manually calculate the elastic moduli. We used a relative calibration method to obtain quantitative results. For the relative calibration, the tip radius was adjusted (for the HOPG data) until the average calculated reduced modulus equaled the nominally reduced modulus of HOPG (~19.2 GPa). The adjusted tip radius considers the physical tip radius and any other factors that affect the calculated reduced elastic modulus. Examples of these include the changes in the spring constant since the factory calibration and any errors in the deflection sensitivity calibration. We used the effective tip radius to calculate the elastic modulus from the experimental data. The Maugis approximation for the DMT model (Derjaguin et al., 1975) was used to analyze the data because it is a good model for the load-displacement behavior of relatively stiff samples. The load, P , and indentation depth, δ are defined as follows:

$$P = \frac{4E\sqrt{R}}{3(1 - \nu^2)}\delta^{3/2} - 2\pi\gamma R \quad (3)$$

$$\delta = \frac{a^2}{R} - \sqrt{\frac{2\pi a \gamma}{E(1 - \nu^2)}} \quad (4)$$

Here, E is the elastic modulus, R is the tip radius, ν is the Poisson's ratio, γ is the surface energy, and a is the contact area. After estimating the elastic moduli, the results were cleaned by discarding all moduli less than 0 GPa and greater than 30 GPa. This removes the unphysical and non-organic results. Additionally, all curves with an R^2 value less than 0.7 were discarded. Although this value of 0.7 is somewhat arbitrary, it was selected to eliminate curves with bad fits, representing <1% of the total data set.

2.5. Scanning electron microscopy and energy dispersive X-ray spectroscopy (SEM-EDS)

All SEM-EDS imaging was performed using a field emission scanning electron microscope (FE-SEM) (Teneo, FED). Following the AFM analysis, a carbon evaporator (K950×, Emitech) was used to coat each shale sample to ensure adequate conductivity for SEM-EDS characterization. The carbon-coated probes were attached to the SEM stage with carbon tape, and the copper tape was applied from the sample surface to the SEM stage to provide excellent conduction. Backscattered electron (BSE) sample mapping was performed using a beam current of 6.4 nA and an accelerating voltage of 20 kV. Using the coordinates and origin from the AFM analysis, the same ROI was identified with well-defined features. Next, SEM-EDS maps were acquired (for the colocalized ROI using a beam current of 6.4 nA and an accelerating voltage of 20 kV) to relate the mechanical property differences observed in the AFM analysis.

3. Results and Discussion

3.1. Geochemistry and mineralogy

Table 2 presents the geochemical parameters and mineral assemblages of the experimental samples. Results from the source rock analysis show an increase in the T_{max} and a decrease in the reactive organic matter (Rock-Eval S_2) with the increase in heating time. The quantity of organic matter is expressed as total organic carbon (TOC) (Hunt and Freeman, 1996). TOC content was found to vary from 8 wt% to 15 wt%, implying that all samples are highly organic-rich. The TOC value shows a decrease of 47% from 0 to 48 h, with increasing T_{max} . This finding is consistent with previous research, which illustrates that the TOC in shales decreases as thermal maturity increases (Peters et al., 2015). The average TOC for the experimental samples is roughly 10% and is significantly higher than the commonly accepted source rock minimum of 0.5% for shales (Tissot and Welte, 1978). Additionally, our results show a significant reduction in HI with increasing thermal maturity (Fig. 4). Fig. 4 is a pseudo-Van Krevelen diagram that shows the relationship between hydrogen/carbon (H/C) and oxygen/carbon (O/C) atomic ratios. The HI is approximately equivalent to the H/C atomic ratio, and the oxygen index (OI) is approximately equivalent to the O/C atomic ratio (Espitalié et al., 1977; Peters, 1986; Baskin, 1997). The HI and OI data are plotted on a pseudo-Van Krevelen diagram and illustrate the range of three major kerogen types (Types I, II, and III) at various maturity levels. The HI and OI plot trend is consistent with previous studies with increasing maturation.

The mineralogy of the experimental samples shows a varying composition. The data reveals that clay minerals (chlorite, illite, kaolinite, and muscovite) and quartz are the predominant minerals in the samples, while K-feldspars (orthoclase and microcline) and albite are the minor minerals. Calcite, dolomite (carbonate minerals), pyrite, and halite are the trace minerals in these samples. The mineralogy of the samples changed in concentration after thermal maturation, with a 36% and 55% decrease in the clay content, a 43% and 75% increase in quartz, and a 62% and 59% increase in K-feldspars for 12 h and 48 h samples, respectively. The results also show that the calcite fraction reduced in volume with increased heating time and thermal maturation, whereas the dolomite fraction increased. This suggests that calcite dissolves more than dolomite.

3.2. Peak force - quantitative nanomechanical mapping (PF-QNM)

3.2.1. Data screening

Scan area of $10 \times 10 \mu\text{m}$ imaging was conducted on each sample, and it provided the desired effect, decreased topography changes with

Table 2
Geochemical parameters and mineral assemblages of the experimental samples.

Sample	TOC (wt%)	T_{max} °C	HI ($S_2 \cdot 100 / TOC$)	qtz	clay	pyr	k-feld	plag	dol	cal	hal	Amp
0-hr	15.28	414	627.93	22.15	34.40	4.40	16.16	2.06	3.18	0.66	0.75	16.24
12-hr	11.06	433	361.26	24.65	39.70	4.75	19.64	4.31	1.04	1.78	0.19	3.93
48-hr	8.60	444	166.07	22.95	38.76	4.75	18.42	4.11	0.47	2.15	0.17	8.48

Note for Minerals: qtz – quartz, clays – (illite, muscovite, kaolinite, chlorite), pyr – pyrite, k-feld – k-feldspars (microcline and orthoclase), plag – plagioclase (albite), dol – dolomite, cal – calcite, hal – halite, Amp – amorphous.

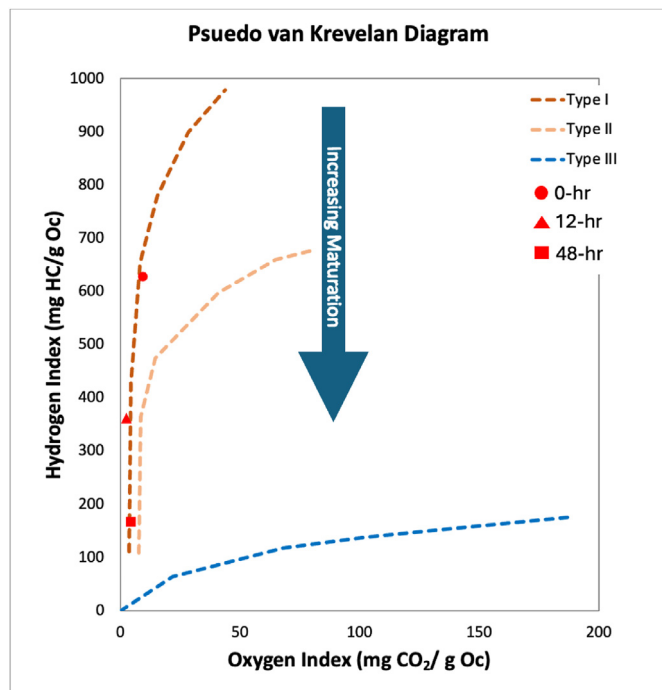


Fig. 4. A pseudo-Van Krevelen plot of the experimental samples shows the kerogen types and changes in kerogen composition with maturation.

increased accuracy of the modulus measurements. The smaller features allowed the tip to track the surface better, and the smaller scan size enabled scanning with fewer samples/lines while maintaining good spatial resolution. This technique worked very well to acquire large volumes of elastic modulus data relatively quickly.

Using the relative calibration method in AtomicJ, the resulting force curves were analyzed and scaled against a highly ordered pyrolytic graphite (HOPG, $E \sim 18$ GPa) standard. The relative calibration and data cleaning procedure were also used on the QNM data. The data cleaning procedure removed less than 1% of the data for the 12-hr and 48-hr samples. The cleaning removed more data from ROI 1 and ROI 3 on

Table 3
Results from numerical analysis using AFM PF-QNM.

Sample	Mean Elastic Modulus (GPa)	Standard Deviation (GPa)	Mean R^2	Skew	N	% Yield	Average Surface Roughness (nm)
0-hr ROI 1	5.38	2.41	0.95		228,841	87.30	122
0-hr ROI 2	6.43	3.06	0.96		261,725	99.84	181
0-hr ROI 3	8.00	5.80	0.89		246,308	93.96	189
0-hr Total	6.03	4.18	0.93	2.19	736,874	93.70	164
12-hr ROI 1	4.68	2.09	0.96		260,898	99.52	211
12-hr ROI 2	6.79	3.45	0.95		261,357	99.70	196
12-hr ROI 3	5.11	2.72	0.96		262,012	99.95	153
12-hr Total	5.53	2.95	0.96	1.49	784,267	99.72	187
48-hr ROI 1	3.44	1.86	0.94		260,720	99.46	175
48-hr ROI 2	3.84	2.11	0.97		261,367	99.70	149
48-hr ROI 3	4.22	2.26	0.96		261,340	99.69	253
48-hr Total	3.83	2.11	0.96	0.92	783,427	99.62	192

the 0-hr sample because the topographical artifacts in those images induced a greater number of higher and lower elastic modulus values. The resulting statistics are summarized in [Table 3](#).

3.2.1.1. Effect of probes used in AFM nanomechanical characterization. This study used two probes, the silicon RTESPA-525 and the diamond-tipped PDNISP. Both probe types have extremely stiff cantilevers (>200 N/m), which allow them to accurately probe the mechanical properties of materials with elastic moduli between 1 and 30 GPa. The RTESPA-525s have a spring constant close to or exceeding that of the PDNISP (226 N/m) and a nominal tip radius of 8 nm, making them less susceptible to wear and tear. The PDNISP has a very stiff stainless-steel cantilever, and its diamond tip is impervious to any wearing. However, its drawback is the low aspect ratio cube corner tip with a nominal tip radius of 40 nm, making the accurate imaging of steep or very small features difficult or impossible. While the PDNISPs come with factory-calibrated spring constants, the RTESPA-525 has special RTESPA-525-30s with a nominal tip radius of 30 nm (instead of 8 nm).

Fig. 5 presents $85 \times 85 \mu\text{m}$ AFM topography images, which show the difference in spatial resolution when using a PDNISP (Left) and a RTESPA-525 (Right). In general, the RTESPA-525 image clearly shows finer details with greater accuracy. An additional problem with the RTESPA-525 probes stems from the fragility of Silicon. Whereas the resulting image (in [Fig. 5](#)) showed great topography, the modulus map shown in [Fig. 6](#) was noisy because the indentation depth was very shallow (~ 6 nm). In contrast, the PDNISP modulus map ([Fig. 6](#)) showed a significant difference between the more complex mineral inclusions and the surrounding matrix, with a deeper average indentation depth (~ 22 nm).

3.2.1.2. Tip wear analysis. Due to the large scale, high resolution, and extensive topographical features, the scan rate was set at the minimum allowable value of 0.1 Hz. With a line period of 10 s and a Peak Force tapping frequency of 2 kHz and 1024 lines, there are over 20 million tip-sample interactions over a single image. Extreme tip wear was caused by a large number of tip-sample interactions in conjunction with the high setpoint needed to accurately track the rough surface and to penetrate deep enough to measure the mechanical properties accurately. A consistent tip radius is necessary across an entire image because the elastic modulus calculated at each point uses the same tip radius the user

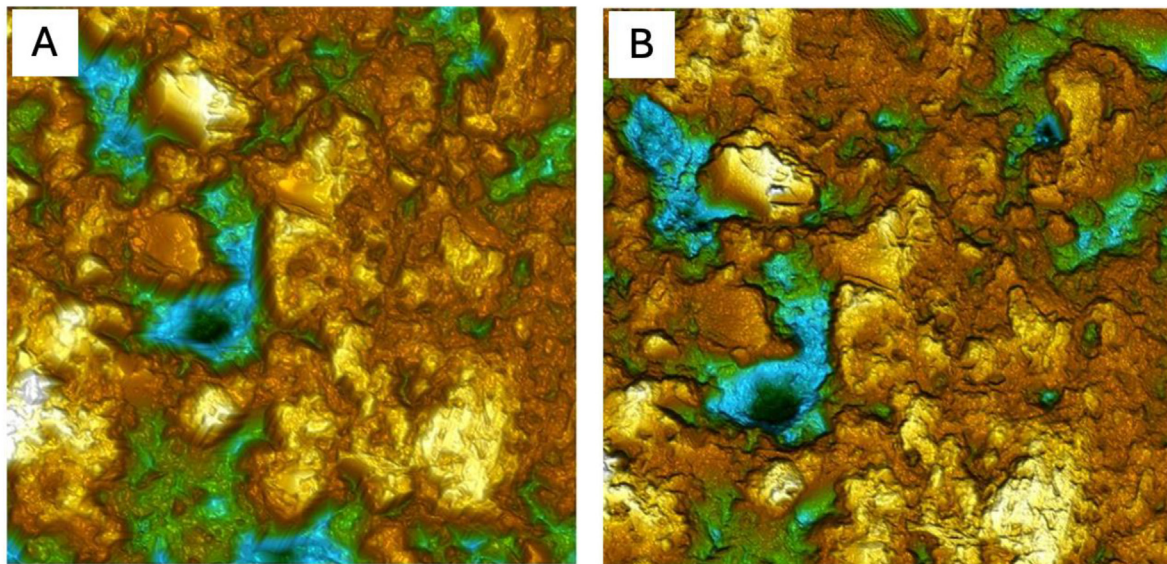


Fig. 5. Topography maps using two different probes: (a) the mapped area using the PDNISP probe; and (b) the modulus map using the RTESPA-525 probe.

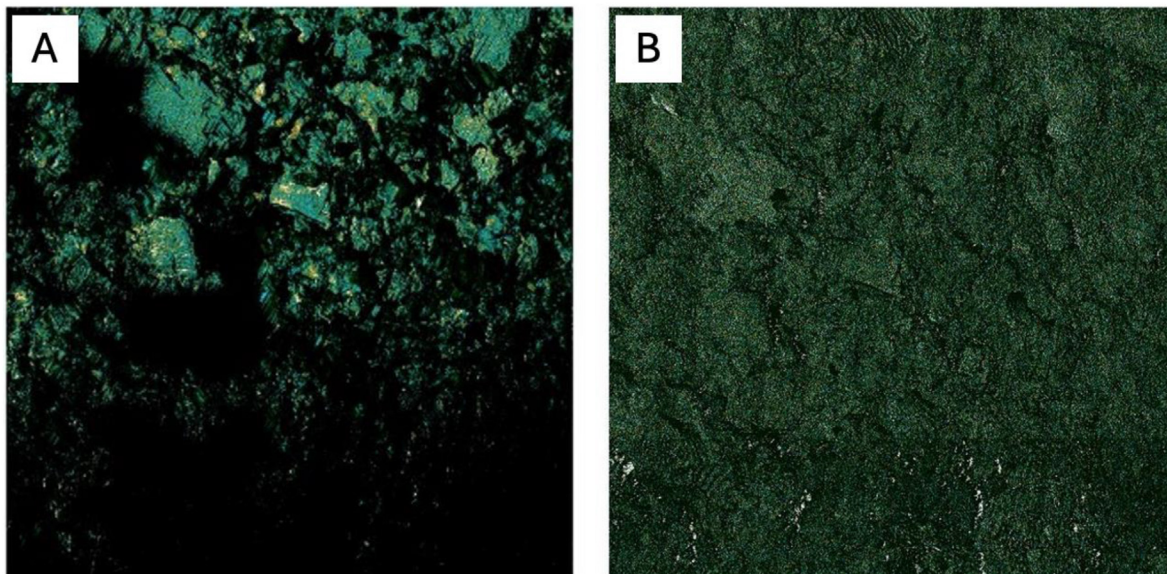


Fig. 6. Modulus maps using two different probes. (a) the mapped area using the PDNISP probe; and (b) the mapped area using the RTESPA-525 probe.

inputs at the beginning of the experiment. If the tip is wearing over the image, the calculated elastic moduli near the end will be significantly overestimated compared to the values calculated at the beginning.

Fig. 7 shows estimated tip models from the tip qualification function in the Nanoscope analysis. The probe tips are used to image TiO_2 nano spikes with sub-nanometer radii of curvature. The TiO_2 rods have the effect of imaging the probe rather than the probe reproducing them. The Nanoscope analysis software picks out tip shapes from the image and develops the models shown. Unfortunately, the high wear observed makes the RTESPA-525 probes unusable for the current experiments, which require a quantitative analysis. In contrast to the heavy wear observed in the silicon RTESPA-525 probes, the diamond-tipped PDNISP probes exhibit no wear even under extensive use. For example, the two models of the same probe tip in Fig. 8 were created a month apart. After over ten images and hundreds of nano-indentations, no wear was observed. The estimated tip radius changed from 29.39 nm to 28.21 nm, which is essentially the same, within the capabilities of the modeling method.

3.2.2. DMT modulus of shale organic matter

It can be observed that the mean elastic modulus decreases with increasing thermal maturing time. About 1% to more than 40% of shales with hydrocarbon source rock potential have a high-volume component of organic matter (Vernik and Nur, 1992). Due to the softness of the organic matter, even a small amount significantly impacts the shale's mechanical behavior (Vernik and Milovac, 2011; Sayers, 2013; Kumar et al., 2015). However, a wide range of measured elastic properties for organic matter has been recorded, which would make it challenging to apply rock physics models. For instance, the kerogen in the Woodford Shale was subjected to nanoindentation studies by Zeszotarski et al. (2004). Assuming linear isotropy with a Poisson's ratio of 0.3, Young's modulus (E) was estimated as 11.5 GPa. The same approach was used by Zargari et al. (2013) and Kumar et al. (2012), who obtained E values less than 2 GPa for very porous kerogen. Vernik and Nur (1992) back-analyzed the mechanical characteristics of kerogen using the thin-layer composite concept. They concluded that it is isotropic, with Young's modulus and Poisson's ratio (ν) values of 8 GPa and 0.28,

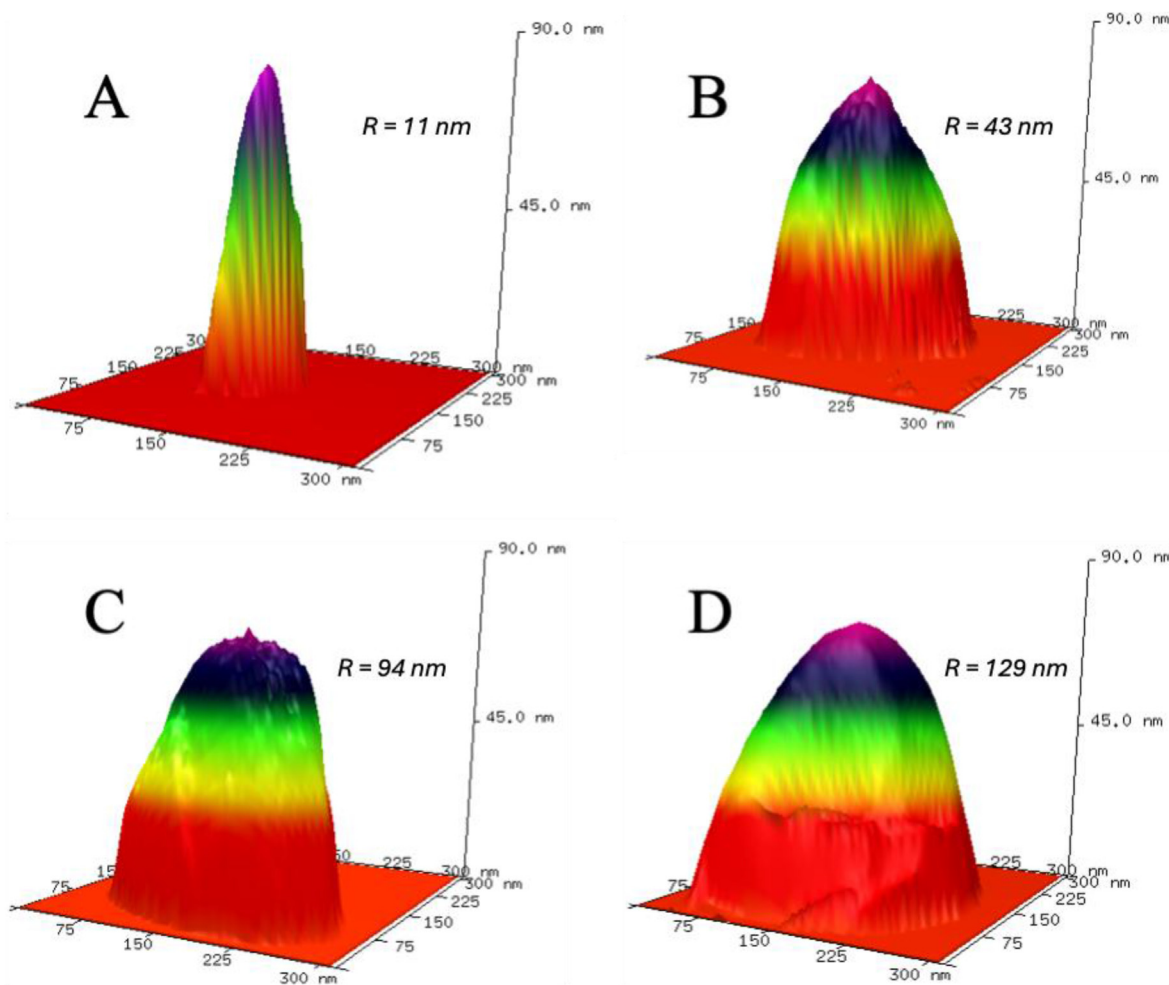


Fig. 7. RTESPA-525 (silicone probe) tip models: (a) out-of-the-box unused tip, (b) after one image, (c) after a second image, and (d) after a third image. It shows the wearing of the tip with each use.

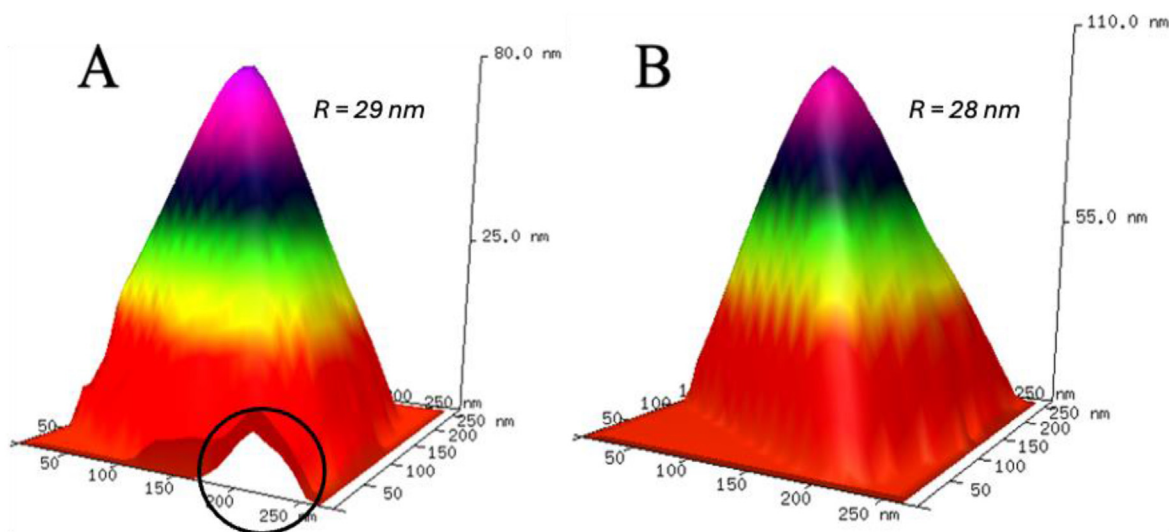


Fig. 8. PDNISP (diamond probe) tip models. (a) Tip as received (out-of-the-box) (b) Tip after over a thousand nanoindents. The models were created a month apart with an estimated tip radius change of 1.18 nm. This implies a negligible wearing of the tip over time. The observed asperity in A, as highlighted by the black circle, is likely either an artifact resulting from the blind tip reconstruction (BTR) method or attributable to the presence of a nanoscale contaminant, such as a dust particle, on the tip's surface.

respectively. Yan and Han (2013) back-calculated Young's modulus for immature, mature, and over-mature organic matter, and obtained 4.5, 6.42, and 10.7 GPa, respectively. Eliyahu et al. (2015) used an atomic force microscope and the PeakForce QNM Rtests to measure Young's modulus of organic materials in a thin piece of shale at the nanoscale. Their results ranged from 0 to 25 GPa, with a median of 15 GPa. According to research by Emmanuel et al. (2016), the elastic modulus of kerogen increases as thermal maturity increases.

Considering that this work focuses on the organic matter in shales (which are identified as the dark areas in SEM images like Fig. 9), it is worth mentioning that the organic matter can sometimes be found mixed within the matrix of a rock in the form of narrow strips. Therefore, it is more difficult to manually extract and interpret the data measured in this phase. In this work, we further examined the elastic moduli of organic matter in the samples. After the topography imaging, we identified the three ROIs shown in Fig. 10, using 4×4 nano indent arrays.

The PF-QNM using the PDNISP probe is reliable after repeated scans with different resolutions produced similar modulus values for the same area. Figs. 11–13 present the topographic images and Young's modulus mapping for the three ROIs after 0, 12, and 48 h, respectively.

Fig. 14 presents the statistical analyses of Young's modulus variable distribution within three ROIs for the 0-, 12-, and 48-hr samples, respectively. The results show three histograms: one for each of the three ROIs, and a comparison of Fig. 14a–c, Fig. 14d–f, and Fig. 14g–i shows that the upper limit of the modulus decreases with the duration of the heating. Fig. 14a–c shows that the organic matter in the 0-hr sample has a modulus that ranges between 2 and 15 GPa, with a peak value of 4 GPa. In contrast, Fig. 14d–f shows that the modulus of organic matter in the 12-hr sample ranges between 1 and 13 GPa, while Fig. 14g–i shows that the organic matter in the 48-hr sample has a modulus of 0–8 GPa. The long positive skew observed on the left side of the histograms in Fig. 14a–c is typical for nanoindentation experiments with many force curves. This is because any elastic modulus value less than zero has no physical meaning in non-vibrating systems since Young's modulus can only be positive. So, the left side of the histogram has a lower limit of 0 GPa, whereas the right side is unconstrained. It is also observed that the skewness of the data decreases with increasing heating time, and the long tail decreases in length from the 0-hr sample to the 48-hr sample.

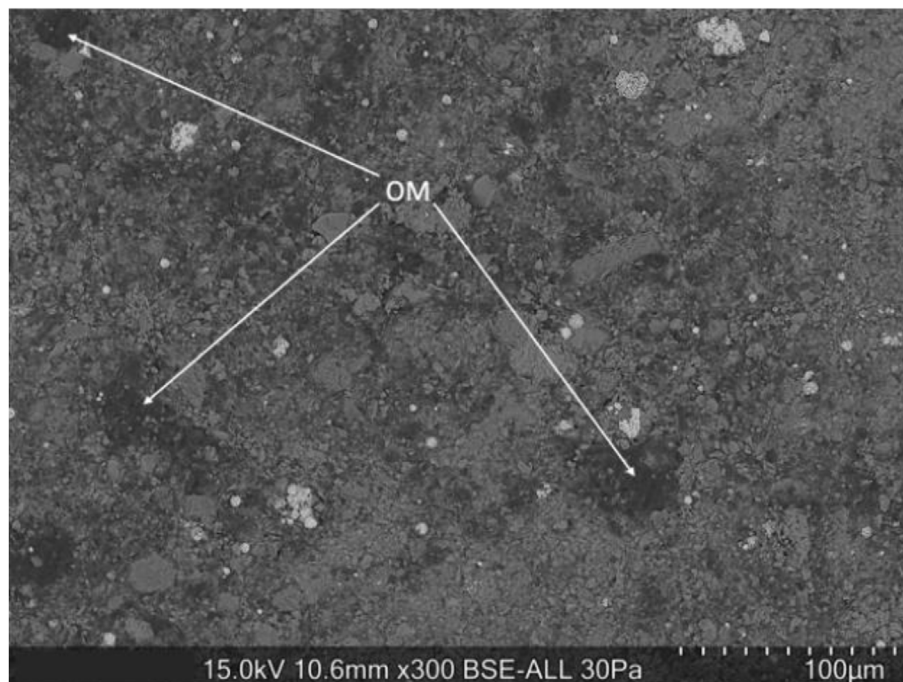


Fig. 9. BSE image showing the Bakken Shale microstructure. The dark areas are organic matter, which is labeled as “OM”.

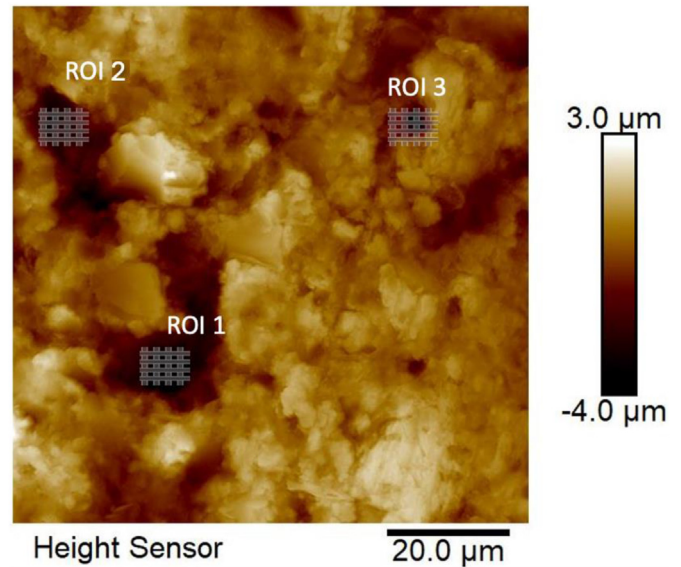


Fig. 10. Topography mapping in shales showing the regions of interest (ROI) using 4×4 nano indent arrays.

Measurements show that organic matter generally has modulus values between 0 and 30 GPa.

The BSE-SEM images were captured with a wider field of view, encompassing the central region of each ROI. Elemental maps from the samples' energy-dispersive X-ray spectroscopy study (EDS) helped distinguish the various phases of the samples. To ensure the existence of specified organic matter and to distinguish it from void spaces or other inorganic phases, the EDS elemental maps for the 48-hr sample overlapped with the DMT Modulus map, as shown in Fig. 15. As expected, non-silicate minerals like pyrite, which can be differentiated from the concentration of Si and Fe in EDS maps correspond to the inorganic phase. The images presented in Fig. 15 show the colocalized AFM and SEM for ROI 1 in the 48-hr sample.

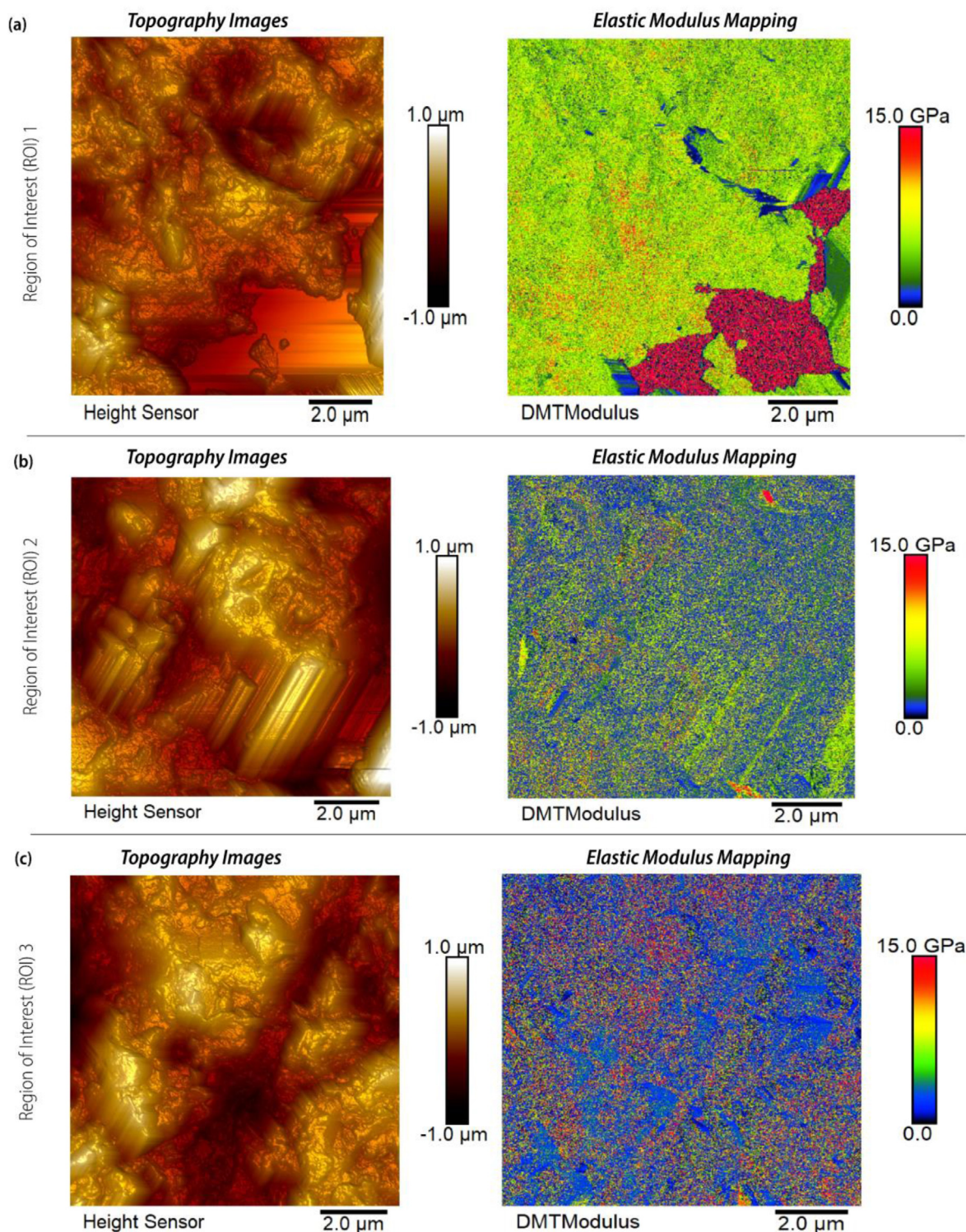


Fig. 11. Topography images and elastic modulus mapping of the three different regions of interest (ROI) for the immature (0-hr) shale: (a) ROI 1, (b) ROI 2, and (c) ROI 3.

3.2.3. Young's modulus of shale organic matter

Equation (2) shows that the estimation of Young's modulus depends on the Poisson's ratio. So, one of the limitations of the AFM PF-QNM technique for estimating the elastic modulus of any material is its dependence on and sensitivity to the assumed value of Poisson's ratio. We used the peak values obtained from the DMT modulus as representative values to calculate Young's modulus for organic matter and assumed a Poisson's ratio of 0.3. Although each mineral has its specific Poisson's

ratio (available in the literature), we have opted for a uniform value of 0.3 for simplicity and consistency across all materials (Griffiths et al., 2012). These results were compared with reported Young's modulus values from previous studies and summarized in Table 4.

Based on the analyses in this study, which are presented in Fig. 16, the average Young's modulus for the immature sample (0-hr) is 6.0 GPa. For the early mature sample (12-hr), the average elastic modulus is 5.5 GPa, whereas, in the peak mature sample, the average elastic modulus is 3.8

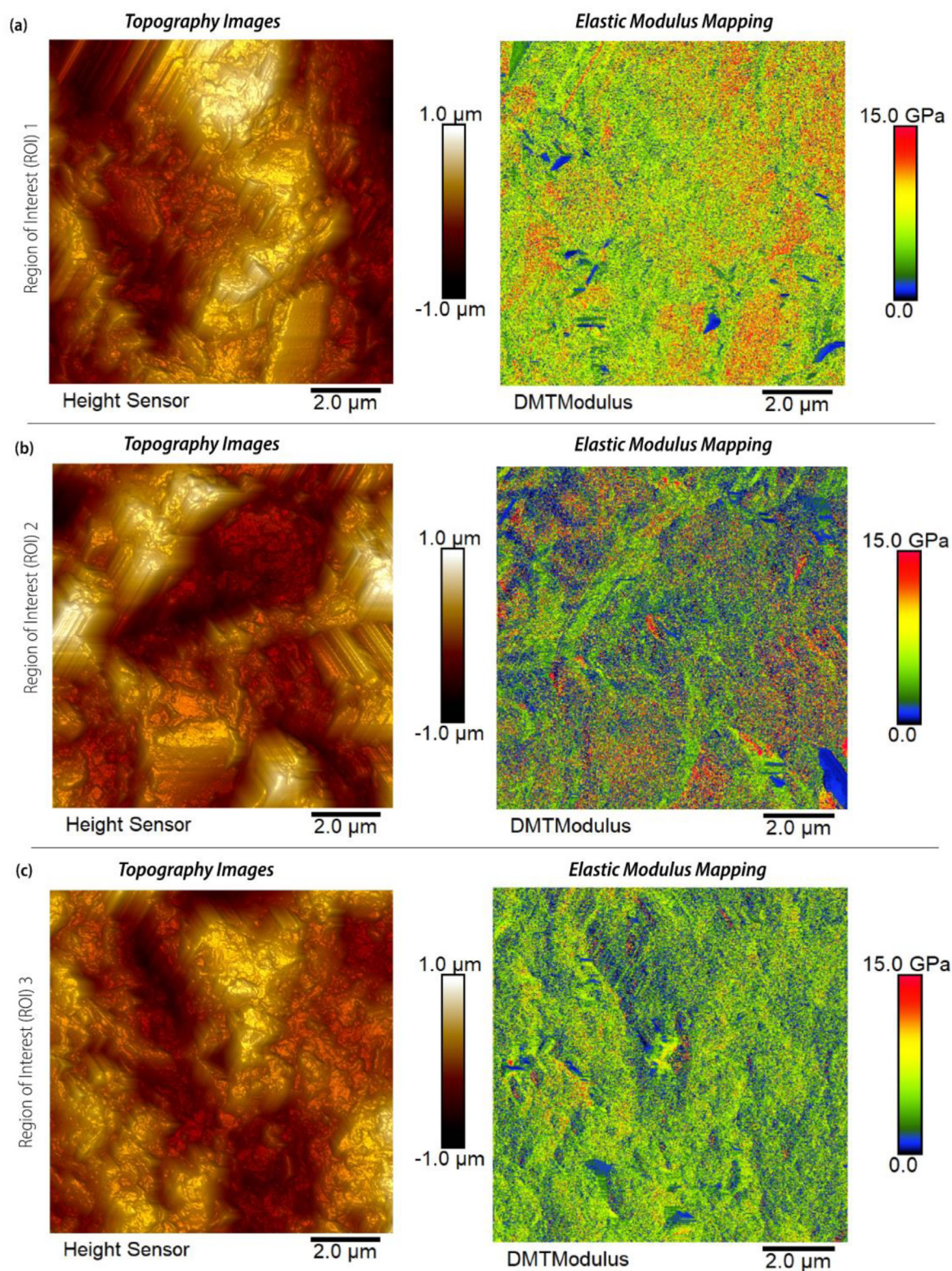


Fig. 12. Topography images and elastic modulus mapping of the three different regions of interest (ROI) for the early-mature (12-hr) shale: (a) ROI 1, (b) ROI 2, and (c) ROI 3.

GPa. Also, the values of Young's modulus for the shale organic matter are within the range of published nanomechanical measurements in organic-rich shales, which range between 5 GPa and 25 GPa (Kumar et al., 2012; Zargari et al., 2013; Eliyahu et al., 2015; Alstadt et al., 2016; Emmanuel et al., 2016; Zargari et al., 2016; Li et al., 2018; Graham et al., 2021; Kong et al., 2021, Table 4).

Relative to the elastic modulus of the immature sample, the results in this study (Fig. 16) suggest a significant mechanical degradation in the properties of the organic matter in shales. An 8% decrease in elastic modulus was obtained after 12 h of thermal maturation to achieve early-maturity. In contrast, a 37% decrease in elastic modulus was obtained after 48 h of thermal maturation to obtain peak maturity. Furthermore,

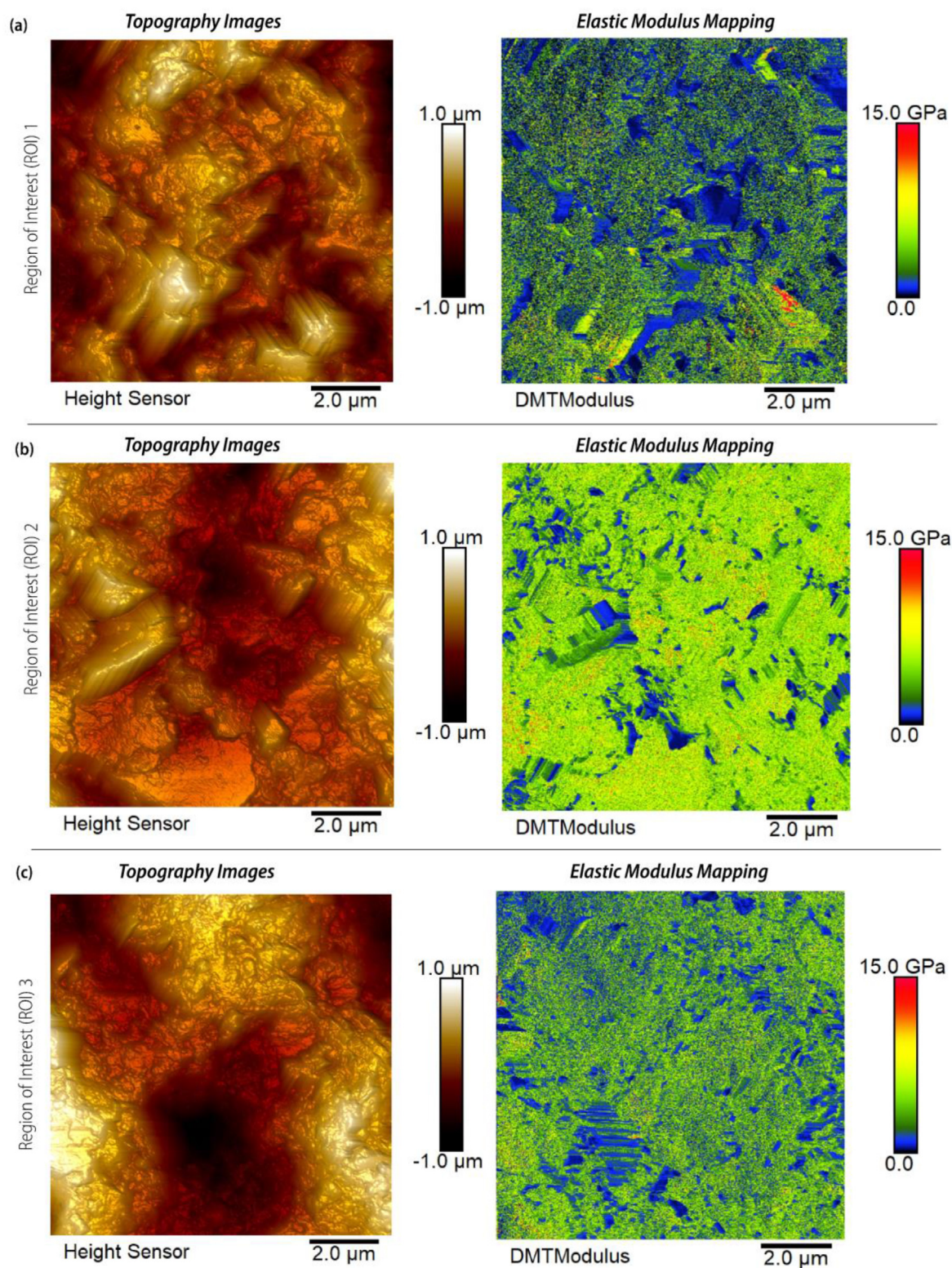


Fig. 13. Topography images and modulus mapping of the three different regions of interest (ROI) for the peak mature (48-hr) shale: (a) ROI 1, (b) ROI 2, and (c) ROI 3.

after the early maturity of organic-rich shales, the heating of the samples for an additional 36 h (to make a total of 48 h) showed that there is a mechanical degradation and weakening of organic matter in shales, which is observable as a 31% reduction in the elastic modulus (Fig. 16).

Two processes occur simultaneously when the shale samples are heated to induce thermal maturity: (1) hydrocarbons are produced

because of the high temperatures, and (2) the volatile hydrocarbons evaporate. These processes result in changes to the elastic characteristics of the samples. The amount of softer material in the samples decreases due to heating and increasing thermal maturity, while more bitumen and hydrocarbon are formed, and some of these are retained. Since bitumen can flow freely on the surface of the samples, modulus measurements

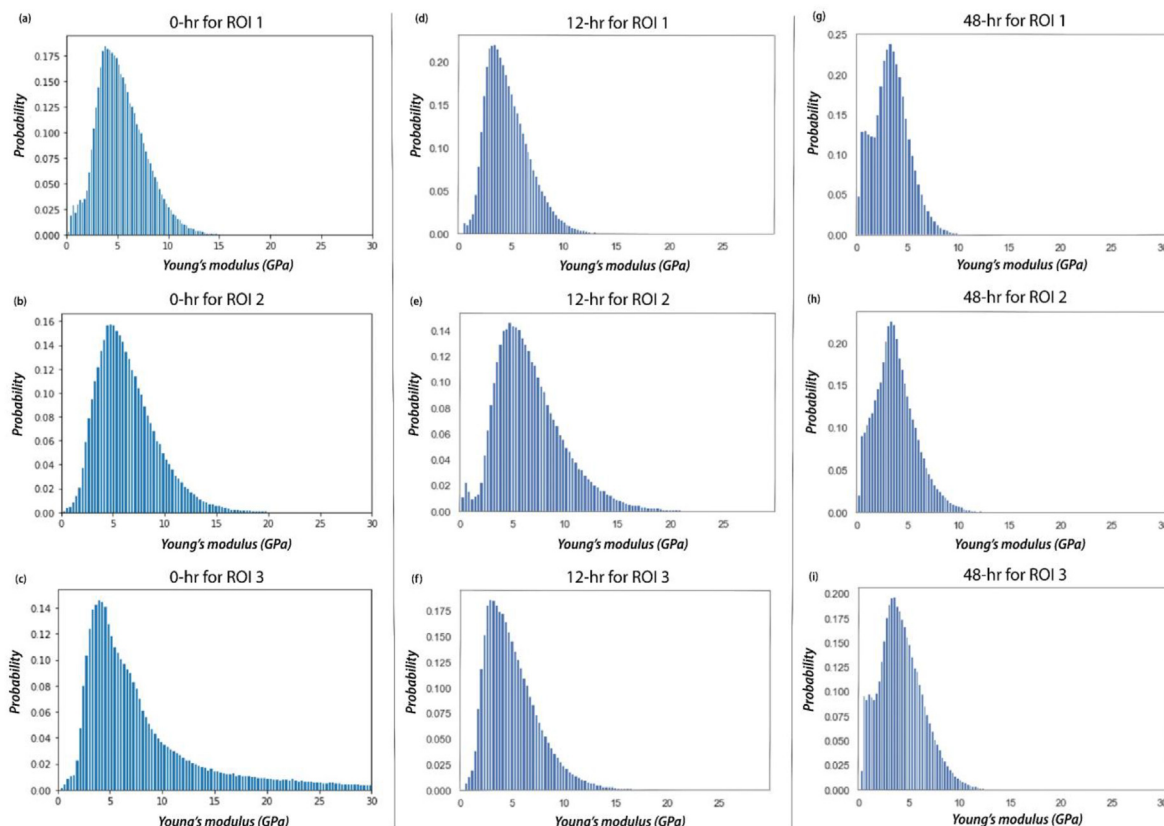


Fig. 14. Statistical analyses of Young's modulus variable distribution within three regions of interest (ROI) for the (a–c) 0-hr sample, (d–f) 12-hr sample, and (g–i) 48-hr sample.

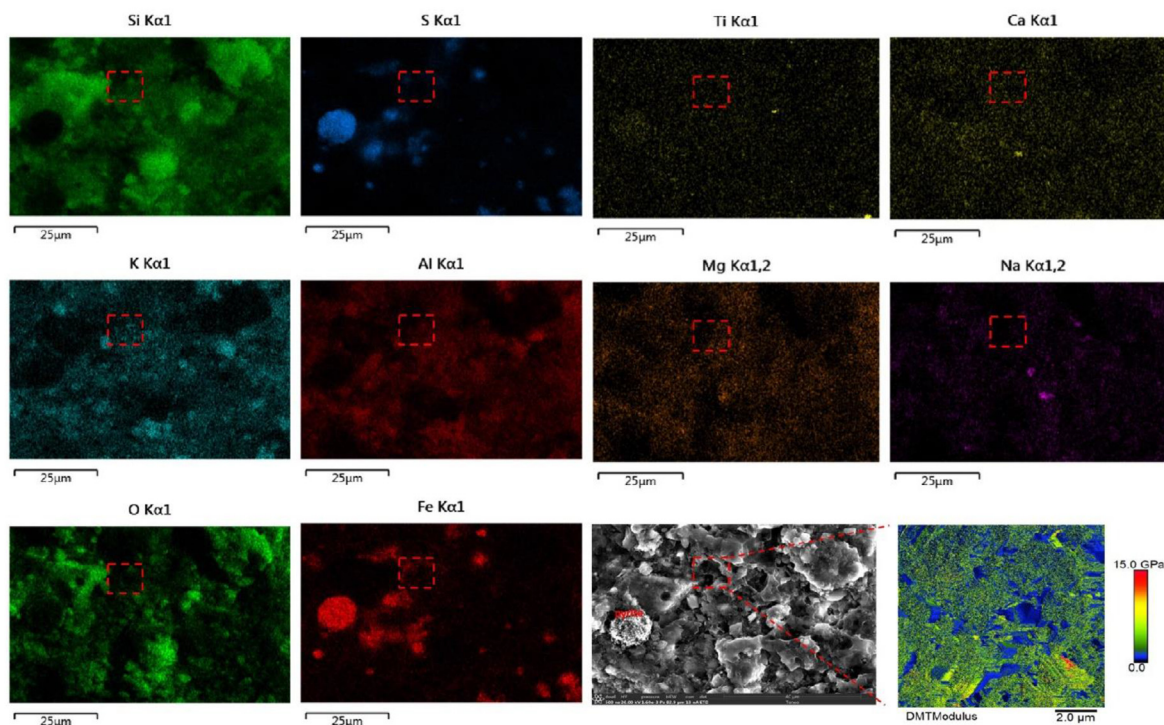
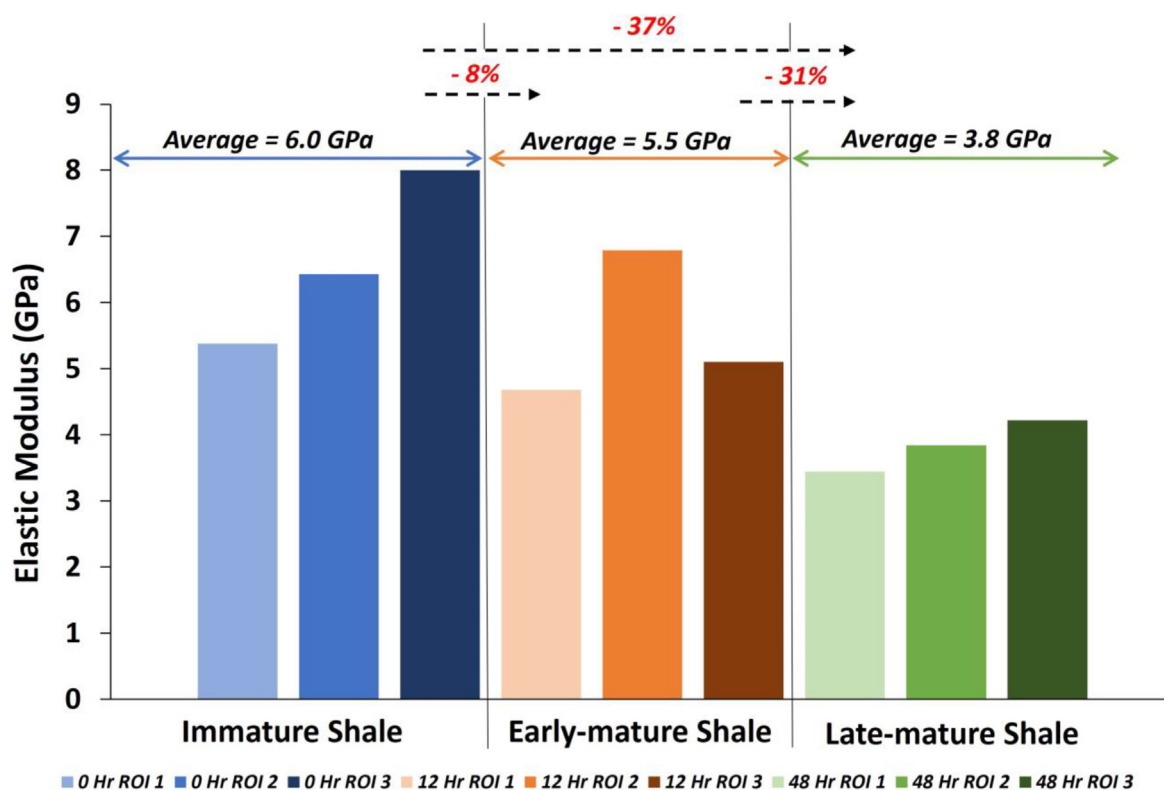


Fig. 15. EDS elemental maps with BSE-SEM images and Young's modulus map for 48-hr ROI 1 showing different phases. The area of EDS maps is the same as the SEM image, while the area within the red rectangle corresponds to the area in Young's modulus map. (For interpretation of the references to colour in this figure legend, the reader is referred to the Web version of this article.)

Table 4

Elastic properties of organic matter in the published literature.

Literature	Formation	Maturity	Assumed ν	OM E (GPa)	Measurement Method
Kumar et al. (2012)	Woodford	High maturity	–	2–10	Nanoindentation
	Kimmeridge	–		6–9	
Zargari et al. (2013)	Bakken	Extruded bitumen	Reduced modulus	2	Nanoindentation
Eliyahu et al. (2015)	Upper Jurassic source rock	High maturity	0.3	2–16	AFM
Alstadt et al. (2016)	Green river oil shale	–	0.25	5–11	Nanoindentation
Emmanuel et al. (2016)	Cretaceous source rock	Low maturity	0.4	3.2–8.7	AFM
Zargari et al. (2016)	Bakken	High maturity	0.3	9.3–29.9	AFM
		Immature kerogen		15–20	Nanoindentation
Li et al. (2018)	Bakken	Mature kerogen	0.3	7–12	Nano-indentation
		Low maturity to high maturity		7–23	AFM
Graham et al. (2021)	–	Dry gas window	–	5–10	AFM and Nanoindentation
Kong et al. (2021)	Bakken	Low maturity to high maturity	0.3	11–18	AFM and Nanoindentation

**Fig. 16.** Estimated elastic moduli of all organic-rich shale samples measured for the three regions of interest (ROIs) under varying thermal maturity periods.

taken at the surface can almost totally probe this low-modulus material. The natural system operates in contradiction to this. A more mature shale sample in a natural system has a higher Young's modulus because more mature samples have less organic material. Additionally, although clay content may not be related to maturity, it also affects the elastic properties (Han et al., 1986).

4. Conclusion

This study used AFM PF-QNM to study the nanomechanical characteristics of shale organic matter in experimental samples with different levels of thermal maturity. The PF-QNM approach provided valuable quantitative and qualitative measurements of the elastic moduli of the organic matter and other constituents of the shale samples studied. The average elastic modulus of the organic matter in immature shale is 6 GPa, whereas those of the early mature and peak mature shales are 5.5 GPa and 3.8 GPa, respectively. This indicates a significant mechanical degradation in organic-rich shales as thermal maturity increases, with a reduction in elastic modulus observed across the maturity stages.

The proposed method used in this study can provide reliable values of elastic moduli of organic matter, which is crucial to the macroscopic behavior of shales. Using the PF-QNM approach indicates a mechanical degradation (immature shale = -8% E ; early mature shale = -31% E ; peak mature shale = -37% E) in organic-rich shales with increasing thermal maturation. The Young's modulus is higher in the immature (0-hr) sample than in the peak mature (48-hr) sample, with a 37% reduction. This observation can be due to low-modulus materials like bitumen, generated during heating, on the surface of the sample being probed during the modulus measurements.

The AFM PF-QNM offers excellent potential for identifying the nanomechanical characteristics of rocks like shales, which have complex and heterogeneous structures. However, this technique requires a more standardized measurement procedure for rocks with a wide range of components and variable moduli.

CRedit authorship contribution statement

Chioma Onwumelu: Writing – review & editing, Writing – original

draft, Methodology, Investigation, Formal analysis, Conceptualization. **Oladoyin Kolawole:** Writing – review & editing, Validation, Investigation, Formal analysis. **Stephan Nordeng:** Validation, Supervision. **Olu-femi Olorode:** Writing – review & editing, Validation.

Declaration of competing interest

The authors declare that they have no known competing financial interests or personal relationships that could have appeared to influence the work reported in this paper.

Acknowledgment

The authors extend their gratitude to Harold Hamm School of Geology and Geological Engineering University of North Dakota for their contribution. Special thanks to Paul Davis and Ashton Enriques at the Micron School of Materials Science & Engineering, Boise State University for sample characterization.

References

- Abedi, S., Slim, M., Hofmann, R., et al., 2016a. Nanochemo-mechanical signature of organic-rich shales: a coupled indentation–EDX analysis. *Acta Geotech* 11, 559–572. <https://doi.org/10.1007/s11440-015-0426-4>.
- Abedi, S., Slim, M., Ulm, F.J., 2016b. Nanomechanics of organic-rich shales: the role of thermal maturity and organic matter content on texture. *Acta Geotech* 11, 775–787. <https://doi.org/10.1007/s11440-016-0476-2>.
- Alstadt, K.N., Kattij, K.S., Katti, D.R., 2016. Nanoscale morphology of kerogen and in situ nanomechanical properties of green river oil shale. *Journal of Nanomechanics and Micromechanics* 6 (1). [https://doi.org/10.1061/\(asce\)nm.2153-5477.0000103](https://doi.org/10.1061/(asce)nm.2153-5477.0000103).
- Asgari, H., Ramezani-pour, A.A., Butt, H.J., 2018. Nano-mechanical behavior of calcium silicate hydrate and calcium hydroxide in cement paste: elevated peak-force study. *Int. J. Civ. Eng.* 16 (3), 273–280. <https://doi.org/10.1007/s40999-016-0125-z>.
- Avseth, P., Mukerji, T., Mavko, G., 2010. *Quantitative Seismic Interpretation: Applying Rock Physics Tools to Reduce Interpretation Risk*. Cambridge university press.
- Baskin, D.K., 1997. Atomic H/C ratio of kerogen as an estimate of thermal maturity and organic matter conversion. *AAPG Bull.* 81 (9), 1437–1450.
- Bobko, C., Ulm, F.J., 2008. The nano-mechanical morphology of shale. *Mech. Mater.* 40 (4–5), 318–337. <https://doi.org/10.1016/j.mechmat.2007.09.006>.
- Dahi-Taleghani, A., Olson, J.E., 2011. Numerical modeling of multistranded-hydraulic-fracture propagation: accounting for the interaction between induced and natural fractures. <http://onepetro.org/SJ/article-pdf/16/03/575/2107035/spe-124884-pa.pdf/1>.
- Derjaguin, B.V., Muller, V.M., Toporov, Y.P., 1975. Effect of contact deformations on the adhesion of particles. *J. Colloid Interface Sci.* 53 (2), 314–326.
- Eliyahu, M., Emmanuel, S., Day-Stirrat, R.J., Macaulay, C.I., 2015. Mechanical properties of organic matter in shales mapped at the nanometer scale. *Mar. Petrol. Geol.* 59, 294–304. <https://doi.org/10.1016/j.marpetgeo.2014.09.007>.
- Emmanuel, S., Eliyahu, M., Day-Stirrat, R.J., Hofmann, R., Macaulay, C.I., 2016. Impact of thermal maturation on nano-scale elastic properties of organic matter in shales. *Mar. Petrol. Geol.* 70, 175–184. <https://doi.org/10.1016/j.marpetgeo.2015.12.001>.
- Espitalié, J., Madec, M., Tissot, B., Mennig, J.J., Leplat, P., 1977. Source rock characterization method for petroleum exploration. In: *In Offshore Technology Conference* (Pp. OTC-2935). OTC.
- Fender, T.D., van der Land, C., Rouainia, M., Graham, S.P., Jones, D.M., Vane, C.H., Wagner, T., 2020. The assessment of organic matter Young's modulus distribution with depositional environment and maturity. *J. Geophys. Res. Solid Earth* 125 (12). <https://doi.org/10.1029/2020JB020435>.
- Gale, J.F.W., Laubach, S.E., Olson, J.E., Eichhubl, P., Fall, A., 2014. Natural fractures in shale: a review and new observations. *AAPG (Am. Assoc. Pet. Geol.) Bull.* 101 (8), 2165–2216. <https://doi.org/10.1306/08121413151>.
- Gerhard, L.C., Anderson, S.B., Lefever, J.A., Carlson, C.G., 1982. Geological development, origin, and energy mineral resources of Williston Basin, North Dakota. *AAPG (Am. Assoc. Pet. Geol.) Bull.* 66 (8), 989–1020.
- Graham, S.P., Rouainia, M., Aplin, A.C., Cubillas, P., Fender, T.D., Armitage, P.J., 2021. Geomechanical characterisation of organic-rich calcareous shale using AFM and nanoindentation. *Rock Mech. Rock Eng.* 54 (1), 303–320. <https://doi.org/10.1007/s00603-020-02261-6>.
- Griffiths, D.V., Paiboon, J., Huang, J., Fenton, G.A., 2012. Homogenization of geomaterials containing voids by random fields and finite elements. *Int. J. Solid Struct.* 49 (14), 2006–2014.
- Han, D.H., Nur, A., Morgan, D., 1986. Effects of porosity and clay content on wave velocities in sandstones. *Geophysics* 51 (11), 2093–2107.
- Hermanowicz, P., Sarna, M., Burda, K., Gabryś, H., 2014. AtomicJ: an open source software for analysis of force curves. *Rev. Sci. Instrum.* 85 (6). <https://doi.org/10.1063/1.4881683>.
- Hua, Y., PeakForce-QNM advanced applications training. Bruker, USA. <https://www.bruker.com/en/products-and-solutions/microscopes/materials-afm/afm-modes/peakforce-qnm.html>.
- Hunt, J.M., Freeman, W.H., et al., 1996. *Petroleum geochemistry and geology*, 2nd Edition, p. 743. New York.
- Khatibi, S., Ostadhassan, M., Tuschel, D., Gentzis, T., Bubach, B., Carvajal-Ortiz, H., 2018. Raman spectroscopy to study thermal maturity and elastic modulus of kerogen. *Int. J. Coal Geol.* 185, 103–118. <https://doi.org/10.1016/j.coal.2017.11.008>.
- Kolawole, O., Oppong, F., 2023. Assessment of inherent heterogeneity effect on continuous mechanical properties of shale via uniaxial compression and scratch test methods. *Rock Mechanics Bulletin* 2 (4), 100065. <https://doi.org/10.1016/j.rockmb.2023.100065>.
- Kong, L., Ostadhassan, M.O., Ling, K., Li, C., Wang, H., 2018. SPE-190058-MS Impact of Thermal Maturation on Wave Velocity in the Bakken Shale. In: <http://onepetro.org/SPEWRM/proceedings-pdf/18WRM/518WRM/D051S015R009/1237318/spe-190058-ms.pdf/1>.
- Kong, L., Hadavimoghaddam, F., Li, C., Liu, K., Liu, B., Semnani, A., Ostadhassan, M., 2021. AFM vs. Nanoindentation: nanomechanical properties of organic-rich Shale. *Mar. Petrol. Geol.* 132. <https://doi.org/10.1016/j.marpetgeo.2021.105229>.
- Kumar, V., Sondergeld, C.H., Rai, C.S., 2012. Nano to macro mechanical characterization of shale. In: *SPE Annual Technical Conference and Exhibition?*, pp. SPE-159804. SPE.
- Kumar, V., Sondergeld, C., Rai, C.S., 2015. Effect of mineralogy and organic matter on mechanical properties of shale. *Interpretation* 3 (3), SV9–SV15.
- Li, C., Ostadhassan, M., Guo, S., Gentzis, T., Kong, L., 2018. Application of PeakForce tapping mode of atomic force microscope to characterize nanomechanical properties of organic matter of the Bakken Shale. *Fuel* 233, 894–910. <https://doi.org/10.1016/j.fuel.2018.06.021>.
- Liu, K., Ostadhassan, M., Bubach, B., Ling, K., Tokhmechi, B., Robert, D., 2018. Statistical grid nanoindentation analysis to estimate macro-mechanical properties of the Bakken Shale. *J. Nat. Gas Sci. Eng.* 53, 181–190. <https://doi.org/10.1016/j.jngse.2018.03.005>.
- Mavko, G., Mukerji, T., Dvorkin, J., 2020. *The Rock Physics Handbook*. Cambridge University Press.
- Ngoma, M.C., Kolawole, O., 2024. Assessment of nano-to-micro-scale geomechanical properties and their time-dependent behavior: current status and progressive perspectives. *Rock Mechanics Bulletin* 3 (1), 100096. <https://doi.org/10.1016/j.rockmb.2023.100096>.
- Niu, Y.F., Yang, Y., Gao, S., Yao, J.W., 2016. Mechanical mapping of the interphase in carbon fiber reinforced poly(ether-ether-ketone) composites using peak force atomic force microscopy: interphase shrinkage under coupled ultraviolet and hydro-thermal exposure. *Polym. Test.* 55, 257–260. <https://doi.org/10.1016/j.polymertesting.2016.09.008>.
- Olorode, O., Wang, B., Rashid, H.U., 2020. Three-Dimensional Projection-Based Embedded Discrete-Fracture model for compositional simulation of fractured reservoirs. *SPE J.* 25 (4), 2143–2161. <https://doi.org/10.2118/201243-pa>.
- Onwumelu, C., Kolawole, O., Bouchakour, I., Ozotta, O., Nordeng, S., Alamootti, M., 2023. CO₂-induced alterations due to thermal maturation in shale: implications for CO₂ utilization and storage. *Greenh. Gases* 13 (6), 797–813. <https://doi.org/10.1002/ghg.2243>.
- Onwumelu, C., Kolawole, O., Nordeng, S., 2021. Maturation-induced modification of organic matter in shales: implications for geological CO₂ storage. *Fuel Commun.* 7, 100009. <https://doi.org/10.1016/j.fueco.2021.100009>.
- Peters, K.E., 1986. Guidelines for evaluating petroleum source rock using programmed pyrolysis. AAPG (Am. Assoc. Pet. Geol.) Bull. <https://doi.org/10.1306/94885688-1704-11d7-8645000102c1865d>.
- Peters, K.E., Burnham, A.K., Walters, C.C., 2015. Petroleum generation kinetics: single versus multiple heating ramp open-system pyrolysis. AAPG (Am. Assoc. Pet. Geol.) Bull. <https://doi.org/10.1306/11141414080>.
- Pittenger, B., Erina, N., Su, C., 2010. *Quantitative Mechanical Property Mapping at the Nanoscale with PeakForce QNM*, vol. 1. Application Note Veeco Instruments Inc, pp. 1–11.
- Sayers, C.M., 2013. The effect of kerogen on the elastic anisotropy of organic-rich shales. *Geophysics* 78 (2), D65–D74.
- Sedin, D.L., Rowlen, K.L., 2001. Influence of tip size on AFM roughness measurements. *Appl. Surf. Sci.* 182 (1–2), 40–48.
- Tissot, B.P., Welte, D.H., 1978. From kerogen to petroleum. In: *Petroleum Formation and Occurrence*. https://doi.org/10.1007/978-3-642-96446-6_10.
- Ulm, F.J., Abusleiman, Y., 2006. The nanogranular nature of shale. *Acta Geotechnica* 1 (2), 77–88. <https://doi.org/10.1007/s11440-006-0009-5>.
- Vernik, L., Milovac, J., 2011. Rock physics of organic shales. *Lead. Edge* 30 (3), 318–323.
- Vernik, L., Nur, A., 1992. Ultrasonic velocity and anisotropy of hydrocarbon source rocks. *Geophysics* 57 (5), 727–735.
- Wang, D., Liang, X., Russell, T.P., Nakajima, K., 2014. Visualization and quantification of the chemical and physical properties at a diffusion-induced interface using AFM nanomechanical mapping. In: *Macromolecules*, vol. 47. American Chemical Society, pp. 3761–3765. <https://doi.org/10.1021/ma500099b>.
- Yan, F., Han, D.H., 2013. Measurement of elastic properties of kerogen. In: *SEG International Exposition and Annual Meeting*. SEG. SEG-2013).
- Zargari, S., Prasad, M., Mba, K.C., Mattson, E.D., 2013. Organic maturity, elastic properties, and textural characteristics of self-resourcing reservoirs Maturity and elastic properties of shales. *Geophysics* 78 (4), D223–D235.
- Zargari, S., Wilkinson, T.M., Packard, C.E., Prasad, M., 2016. Effect of thermal maturity on elastic properties of kerogen. *Geophysics* 81 (2), M1–M6. <https://doi.org/10.1190/GEO2015-0194.1>.
- Zeszotarski, J.C., Chromik, R.R., Vinci, R.P., Messmer, M.C., Michels, R., Larsen, J.W., 2004. Imaging and mechanical property measurements of kerogen via nanoindentation. *Geochem. Cosmochim. Acta* 68 (20), 4113–4119.